

# SCIENTIFIC REPORTS



OPEN

## Na-ion Storage Performances of $\text{FeSe}_x$ and $\text{Fe}_2\text{O}_3$ Hollow Nanoparticles-Decorated Reduced Graphene Oxide Balls prepared by Nanoscale Kirkendall Diffusion Process

Received: 20 November 2015

Accepted: 15 February 2016

Published: 29 February 2016

Gi Dae Park<sup>1</sup>, Jung Sang Cho<sup>1</sup>, Jung-Kul Lee<sup>2</sup> & Yun Chan Kang<sup>1</sup>

Uniquely structured  $\text{FeSe}_x$ -reduced graphene oxide (rGO) composite powders, in which hollow  $\text{FeSe}_x$  nanoparticles are uniformly distributed throughout the rGO matrix, were prepared by spray pyrolysis applying the nanoscale Kirkendall diffusion process. Iron oxide-rGO composite powders were transformed into  $\text{FeSe}_x$ -rGO composite powders by a two-step post-treatment process. Metallic Fe nanocrystals formed during the first-step post-treatment process were transformed into hollow  $\text{FeSe}_x$  nanoparticles during the selenization process. The  $\text{FeSe}_x$ -rGO composite powders had mixed crystal structures of FeSe and  $\text{FeSe}_2$  phases. A rGO content of 33% was estimated from the TG analysis of the  $\text{FeSe}_x$ -rGO composite powders. The  $\text{FeSe}_x$ -rGO composite powders had superior sodium-ion storage properties compared to those of the  $\text{Fe}_2\text{O}_3$ -rGO composite powders with similar morphological characteristics. The discharge capacities of the  $\text{FeSe}_x$ - and  $\text{Fe}_2\text{O}_3$ -rGO composite powders for the 200<sup>th</sup> cycle at a constant current density of  $0.3 \text{ A g}^{-1}$  were 434 and  $174 \text{ mA h g}^{-1}$ , respectively. The  $\text{FeSe}_x$ -rGO composite powders had a high discharge capacity of  $311 \text{ mA h g}^{-1}$  for the 1000<sup>th</sup> cycle at a high current density of  $1 \text{ A g}^{-1}$ .

Transition metal chalcogenides (metal sulfides, selenides, and tellurides) have attracted considerable attention owing to their excellent properties and wide applications in various application fields including energy storage<sup>1–23</sup>. Transition metal sulfides with various compositions have been studied as efficient anode and cathode materials for lithium- and sodium-ion batteries<sup>10–14</sup>. Recently, metal selenides have also been studied as anode materials for lithium- and sodium-ion batteries<sup>15–23</sup>. Metal selenides showed better electrochemical properties than their corresponding metal oxides for anode materials for Na-ion batteries (NIBs).

Nanostructured materials of metal selenides, such as  $\text{MoSe}_x$ ,  $\text{NiSe}_x$ ,  $\text{FeSe}_x$ ,  $\text{SnSe}_x$ ,  $\text{CuSe}_x$ , and  $\text{GeSe}_x$ , prepared mainly by a liquid solution process, have been studied to improve their sodium-ion storage properties by improving the structural stability during repeated sodium charge and discharge processes<sup>19–23</sup>. The combination of nanostructured metal selenides and carbon-based materials, such as amorphous carbon, graphitic carbon, and graphene, is considered an effective method for developing efficient NIB anode materials<sup>22,23</sup>. In particular, graphene and reduced graphene oxide (rGO), which have superior electrical conductivity and high mechanical strength compared to other carbon-based materials, have been successfully applied as support materials of nanostructured metal selenides, including nanopowders, nanoflowers, and nanoplates<sup>24–27</sup>.

Among the metal selenides, iron selenides, which are known to exist, i.e.,  $\text{FeSe}_2$  (cubic and orthorhombic structure), FeSe (hexagonal and tetragonal), and  $\text{Fe}_7\text{Se}_8$  (trigonal), have relatively high conductivity and are

<sup>1</sup>Department of Materials Science and Engineering, Korea University, Anam-Dong, Seongbuk-Gu, Seoul 136-713, Republic of Korea. <sup>2</sup>Department of Chemical Engineering, Konkuk University, 1 Hwayang-Dong, Gwangjin-Gu, Seoul 143-701, Republic of Korea. Correspondence and requests for materials should be addressed to J.-K.L. (email: jkrhee@konkuk.ac.kr) or Y.C.K. (email: yckang@korea.ac.kr)

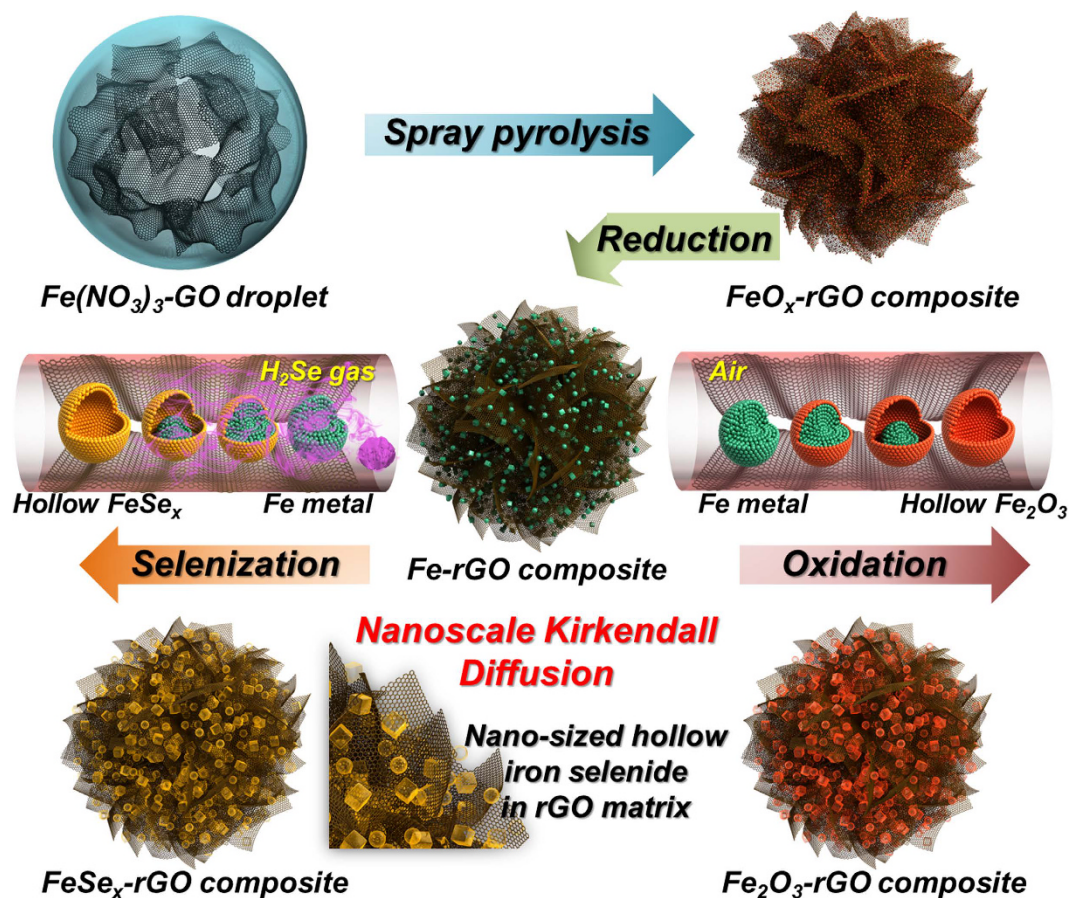


**Figure 1.** Formation mechanism of the hollow  $\text{FeSe}_x$  nanoparticles- and the hollow  $\text{Fe}_2\text{O}_3$  nanoparticles-decorated rGO composite powders by nanoscale Kirkendall diffusion.

more advantageous as electrode materials for NIBs because iron is abundant, inexpensive, and environmentally friendly. Zhang *et al.* reported  $\text{FeSe}_2$  microspheres assembled by nanooctahedra prepared via a simple hydrothermal method. The  $\text{FeSe}_2$  microspheres delivered a stable discharge capacity of  $372 \text{ mA h g}^{-1}$  after 2000 cycles at  $1 \text{ A g}^{-1}$ <sup>28</sup>. However, to the best of our knowledge, the synthesis of nanostructured iron selenide materials and their electrochemical properties as NIB anode materials have not been reported. In addition, iron selenide-graphene (or rGO) composite materials have also not been studied.

In this study, uniquely structured  $\text{FeSe}_x$ -rGO composite powders were prepared by spray pyrolysis and subsequent selenization. Iron oxide-rGO composite powders prepared by spray pyrolysis were transformed into  $\text{FeSe}_x$ -rGO composite powders, in which  $\text{FeSe}_x$  hollow nanoparticles were uniformly distributed throughout the rGO matrix. The iron oxide transformed into hollow  $\text{FeSe}_x$  nanoparticles through metallic iron nanopowders by a two-step post-treatment. Densely structured metallic iron nanopowders were transformed into hollow  $\text{FeSe}_x$  nanoparticles by the well-known nanoscale Kirkendall diffusion process during the selenization process by applying  $\text{H}_2\text{Se}$  gas. The electrochemical properties and Na-ion storage of the uniquely structured  $\text{FeSe}_x$ -rGO composite powders were compared with  $\text{Fe}_2\text{O}_3$ -rGO composite powders with similar morphological characteristics.

## Results and Discussion

The formation mechanism of the hollow  $\text{FeSe}_x$  nanoparticles-decorated rGO composite and the hollow  $\text{Fe}_2\text{O}_3$  nanoparticles-decorated rGO composite powders by spray pyrolysis with nanoscale Kirkendall diffusion is described in Fig. 1. Crumpled rGO powders decorated with iron oxide nanocrystals were prepared by the spray pyrolysis from a colloidal solution containing GO nanosheets and iron nitrate nonahydrate. Iron oxide-rGO composite powders were transformed into  $\text{FeSe}_x$ -rGO composite powders, in which hollow  $\text{FeSe}_x$  nanoparticles were uniformly distributed throughout the rGO matrix, by a two-step post-treatment process. The first step of the post-treatment process at  $400^\circ\text{C}$  under a reducing atmosphere produced metallic iron-rGO composite powders, in which metallic Fe nanocrystals were uniformly distributed throughout the rGO matrix. The second step of the post-treatment process at  $300^\circ\text{C}$  under  $\text{H}_2\text{Se}$  gas produced uniquely structured  $\text{FeSe}_x$ -rGO composite powders. Metallic Fe nanocrystals were transformed into hollow  $\text{FeSe}_x$  nanoparticles during the selenization process by the well-known nanoscale Kirkendall diffusion process. In the early stage of the selenization process, a gas impermeable  $\text{FeSe}_x$  thin layer was formed over the metallic Fe nanocrystals. Subsequently, ion diffusion became the dominant process for further selenization. Fe cations with small radii ( $\text{Fe}^{2+} = 76 \text{ pm}$ ,  $\text{Fe}^{3+} = 65 \text{ pm}$ ) diffused outward more quickly than the larger selenium anions ( $184 \text{ pm}$ ) diffused inward. A new layer of iron

selenide formed over the surface of the preformed  $\text{FeSe}_x$  layer. The diffusion out of the Fe cations during the selenization process formed the nanovoids inside the nanoparticle. The nanovoids formed inside the nanoparticle by nanoscale Kirkendall diffusion segregated into one nanovoid by complete transformation of metallic Fe into  $\text{FeSe}_x$  by selenization process. Finally,  $\text{FeSe}_x$ -rGO composite powders, in which hollow  $\text{FeSe}_x$  nanoparticles were uniformly distributed throughout the rGO matrix, were prepared by a simple two-step post-treatment process at low temperatures. In the same way, the hollow  $\text{Fe}_2\text{O}_3$  nanoparticles were prepared by nanoscale Kirkendall diffusion segregated into one nanovoid by complete transformation of metallic Fe into  $\text{Fe}_2\text{O}_3$  by oxidation process at air atmospheres.

The morphologies of the powders obtained before and after reduction are shown in Figs S2 and 2, respectively. The powders directly prepared by spray pyrolysis had non-crystalline structure, as shown by the XRD pattern in Fig. S3, because of the short residence time of the powders inside the hot wall reactor maintained at 400 °C for 14 s. The sharp peaks of the metallic Fe phase were observed in the XRD pattern of the powders obtained after reduction. The crumpled structure formed by spray pyrolysis was still maintained even after the reduction process, as shown by SEM images in Figs S2 and 2. The iron oxide nanocrystals covered with rGO sheets were not observed in the high-resolution SEM image shown in Fig. S2b. However, the ultrafine nanocrystals distributed inside the crumpled rGO were observed in the high-resolution SEM image shown in Fig. 2b. The TEM images shown in Fig. 2 revealed the metallic iron-rGO composite powders. Ultrafine nanopowders with a core-shell structure were uniformly distributed throughout the crumpled rGO matrix. The ultrafine metallic Fe nanocrystals had high oxidation characteristics even at a room temperature in air. Therefore, the surface oxidation of the metallic Fe nanocrystals dispersed within the rGO matrix formed the  $\text{Fe}_2\text{O}_3$  layer. The further oxidation by nanoscale Kirkendall diffusion formed the void ring within the nanopowders, as indicated by arrows in Fig. 2c. The high resolution TEM image in Fig. 2d showed clear lattice fringes separated by 0.20 and 0.25 nm, which correspond to the (110) and (311) crystal planes of metallic Fe and  $\text{Fe}_2\text{O}_3$  phases, respectively. The SAED pattern and elemental mapping images shown in Fig. 2e,f, respectively, also confirmed the formation of  $\text{Fe}_2\text{O}_3$ -coated metallic Fe nanocrystals by oxidation of metallic Fe nanocrystals.

The morphologies and elemental mapping images of the  $\text{FeSe}_x$ -rGO composite powders obtained after selenization at 300 °C for 6 h with the metallic iron-rGO composite powders are shown in Fig. 3. The SEM image shown in Fig. 3a shows morphologies similar to those of the metallic Fe-rGO composite powders. However, the TEM images shown in Fig. 3b–d show the unique structure of the  $\text{FeSe}_x$ -rGO composite powders, in which hollow nanoparticles formed by nanoscale Kirkendall diffusion are uniformly distributed throughout the rGO matrix. The high-resolution TEM image in Fig. 3d shows clear lattice fringes separated by 0.31 and 0.34 nm, which correspond to the (011) and (001) crystal planes of the  $\text{FeSe}_x$  phase and rGO, respectively. Some of the hollow  $\text{FeSe}_x$  nanoparticles had a rectangular shape in the TEM image, shown as an inset image in Fig. 3c. The metallic Fe crystal growth during the long reduction process changed the spherical morphology into a rectangular parallelepiped morphology. The XRD pattern shown in Fig. S3 revealed the complete conversion of the metallic Fe into iron selenide with mixed crystal structures of FeSe and  $\text{FeSe}_2$  phases after selenization for 6 h. The SAED pattern and elemental mapping images shown in Fig. 3e,f, respectively, also confirmed the formation of  $\text{FeSe}_x$ -rGO composite powders by complete selenization.

The chemical state and molecular environment of the XPS spectra of the  $\text{FeSe}_x$ -rGO composite powders obtained after selenization at 300 °C for 6 h were characterized by X-ray photoelectron spectroscopy (XPS). The XPS survey spectrum in Fig. 4a of the  $\text{FeSe}_x$ -rGO composite powders confirmed the presence of Fe, Se, and C signals. In the Fe 2p spectrum of the  $\text{FeSe}_x$ -rGO composite powders, shown in Fig. 4b, the main peaks observed occurred at binding energies of 710.5 eV for Fe 2p<sub>3/2</sub> and 724.2 eV for Fe 2p<sub>1/2</sub>; these are characteristic of iron selenide (FeSe) and two shake-up satellites<sup>30</sup>. The Se 3d spectrum of the  $\text{FeSe}_x$ -rGO composite powders, shown in Fig. 4c, showed main two peaks located at 54.55 eV (Se 3d<sub>5/2</sub>) and 55.31 eV (Se 3d<sub>3/2</sub>), which are also consistent with iron selenides (FeSe and  $\text{FeSe}_2$ )<sup>31</sup>. The Se–Se and Se–O bonds observed in Fig. 4c revealed the existence of metallic Se and  $\text{SeO}_2$  impurities formed during the selenization process<sup>31</sup>. The C1s peaks shown in Fig. 4d can be attributed to sp<sup>2</sup>-bonded carbon (C–C), epoxy and alkoxy groups (C–O), and carbonyl and carboxylic (C=O) groups, which correspond to peaks at 284.9, 286.7, and 287.6 eV, respectively<sup>32</sup>. The sharp XPS peak at 284.6 eV indicated the thermal reduction of GO into rGO during the preparation process of the  $\text{FeSe}_x$ -rGO composite powders. The TG curve of the  $\text{FeSe}_x$ -rGO composite powders shown in Fig. S4 revealed a one-step weight increase and one-step weight loss for temperatures below 800 °C. The conversion reaction of  $\text{FeSe}_x$  into  $\text{FeSeO}_x$  resulted in a weight increase at 150 °C. The weight loss observed at around 350 °C was attributed to the decomposition of  $\text{FeSe}_x$  and  $\text{FeSeO}_x$  into  $\text{Fe}_2\text{O}_3$  and the combustion of rGO. A rGO content of 33% was estimated from the TG analysis of the  $\text{FeSe}_x$ -rGO composite powders. The morphologies of the  $\text{FeSe}_x$ -rGO composite powders obtained after selenization at 300 °C for 1 h are shown in Fig. S5. The conversion of the metallic Fe nanocrystals into  $\text{FeSe}_x$  hollow nanopowders by nanoscale Kirkendall diffusion occurred even at a short selenization time of 1 h. The overall  $\text{FeSe}_x$  nanopowders decorated within the rGO matrix had spherical and hollow morphologies. The XRD pattern of the composite powders obtained after selenization for 1 h shown in Fig. S6 revealed the minor peaks of the  $\text{Fe}_2\text{O}_3$  phase.

The morphologies of the  $\text{Fe}_2\text{O}_3$ -rGO composite powders prepared as the comparison sample are shown in Fig. 5. The metallic Fe-rGO composite was post-treated at 300 °C for 6 h in air. Metallic Fe nanocrystals transformed into hollow  $\text{Fe}_2\text{O}_3$  nanoparticles by nanoscale Kirkendall diffusion. Therefore, in the TEM images shown in Fig. 5, hollow  $\text{Fe}_2\text{O}_3$  nanoparticles were uniformly distributed throughout the crumpled rGO matrix. The high resolution TEM image in Fig. 5d showed clear lattice fringes separated by 0.25 nm, which correspond to the (311) crystal planes of the  $\gamma$ - $\text{Fe}_2\text{O}_3$  phase. The XRD pattern, SAED pattern, and elemental mapping images shown in Figs S3 and 5e,f, respectively, confirmed the formation of  $\text{Fe}_2\text{O}_3$ -rGO composite powders by complete oxidation.

The electrochemical properties of the hollow  $\text{FeSe}_x$ - and  $\text{Fe}_2\text{O}_3$ -decorated rGO composite powders for sodium-ion storage are shown in Fig. 6. The cyclic voltammograms (CVs) of the  $\text{FeSe}_x$ -rGO and  $\text{Fe}_2\text{O}_3$ -rGO

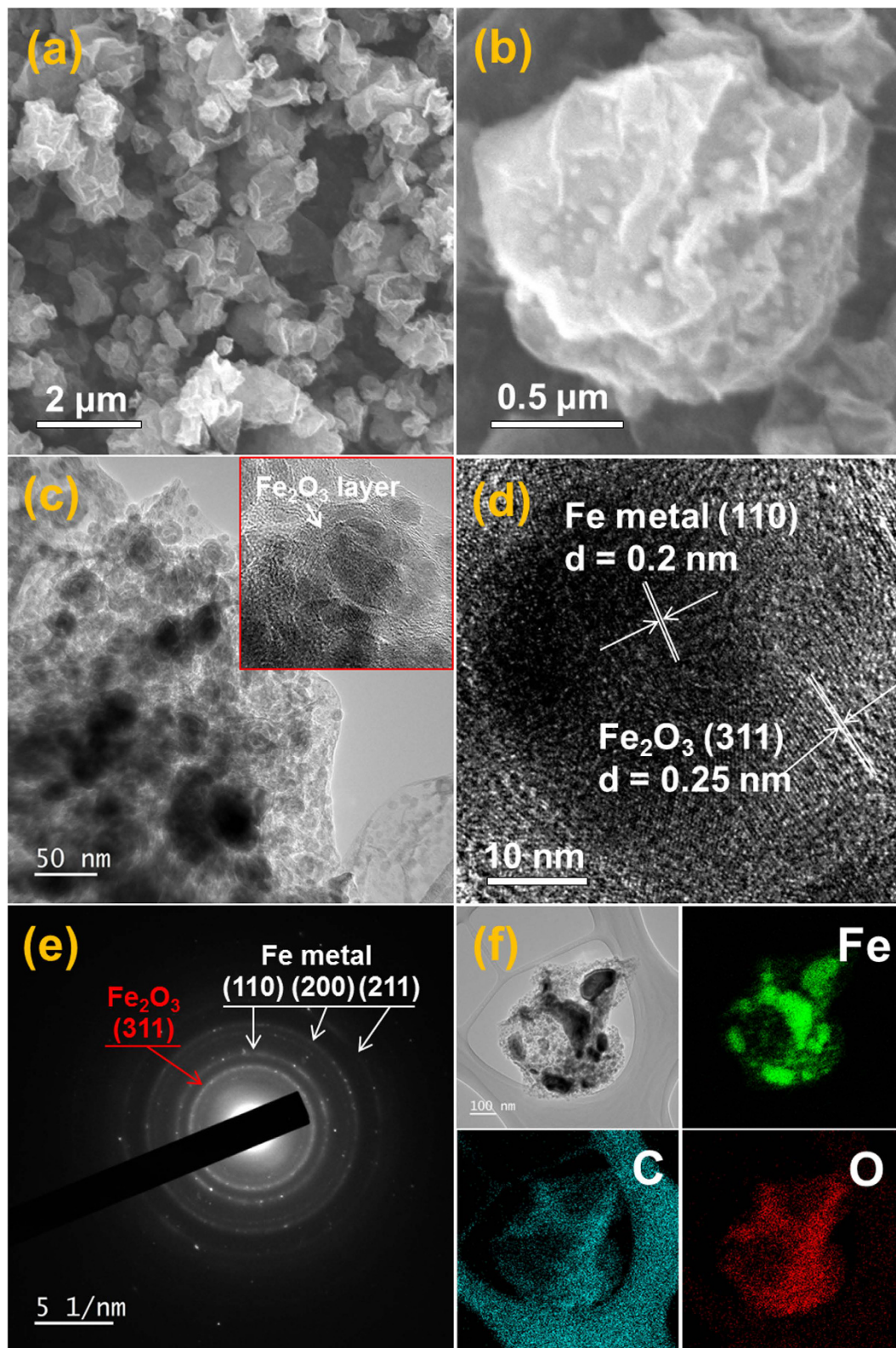


**Figure 2.** Morphologies, SAED pattern, and elemental mapping images of metallic iron-decorated rGO composite powders: (a,b) SEM image, (c) TEM image, (d) HR-TEM image, (e) SAED pattern, and (f) elemental mapping images.

composite powders obtained by post-treatment in  $\text{H}_2\text{Se}$  and air for 6 h during the first five cycles at a scan rate of  $0.1 \text{ mV s}^{-1}$  in the voltage range of 0.001–3 V are shown in Fig. 6a,b, respectively. The first cathodic scan of the

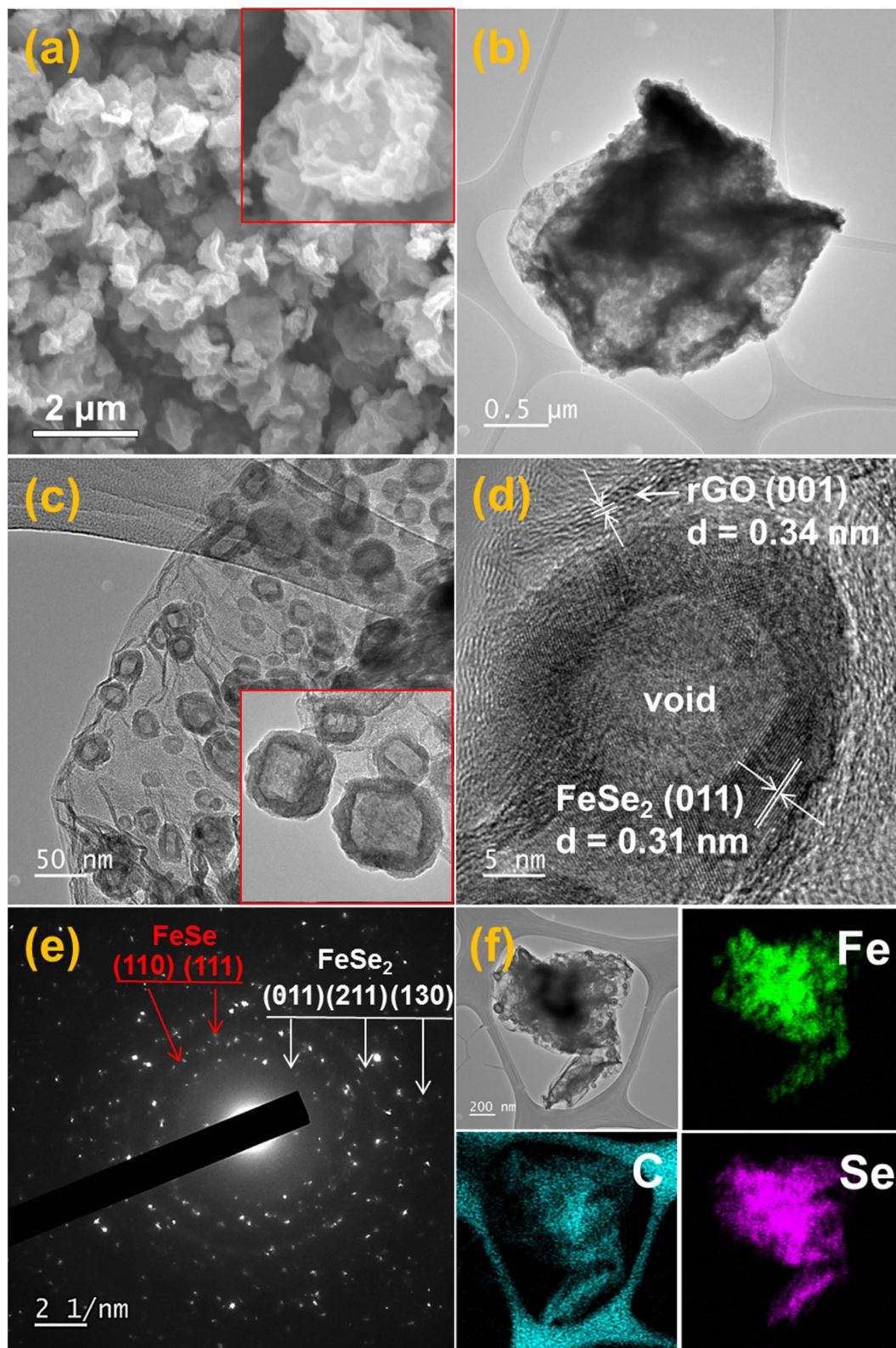


**Figure 3.** Morphologies, SAED pattern, and elemental mapping images of the hollow  $\text{FeSe}_x$ -decorated rGO composite powders obtained by nanoscale Kirkendall diffusion: (a) SEM image, (b,c) TEM images, (d) HR-TEM image, (e) SAED pattern, and (f) elemental mapping images.

$\text{FeSe}_x$ -rGO composite powders showed four distinct peaks located at 1.5, 1.3, 0.8, and 0.4 V. The two sharp reduction peaks located at 1.5 and 1.3 were attributed to the formation of  $\text{Na}_x\text{FeSe}_2$  and  $\text{Na}_x\text{FeSe}$ , respectively<sup>28</sup>. The

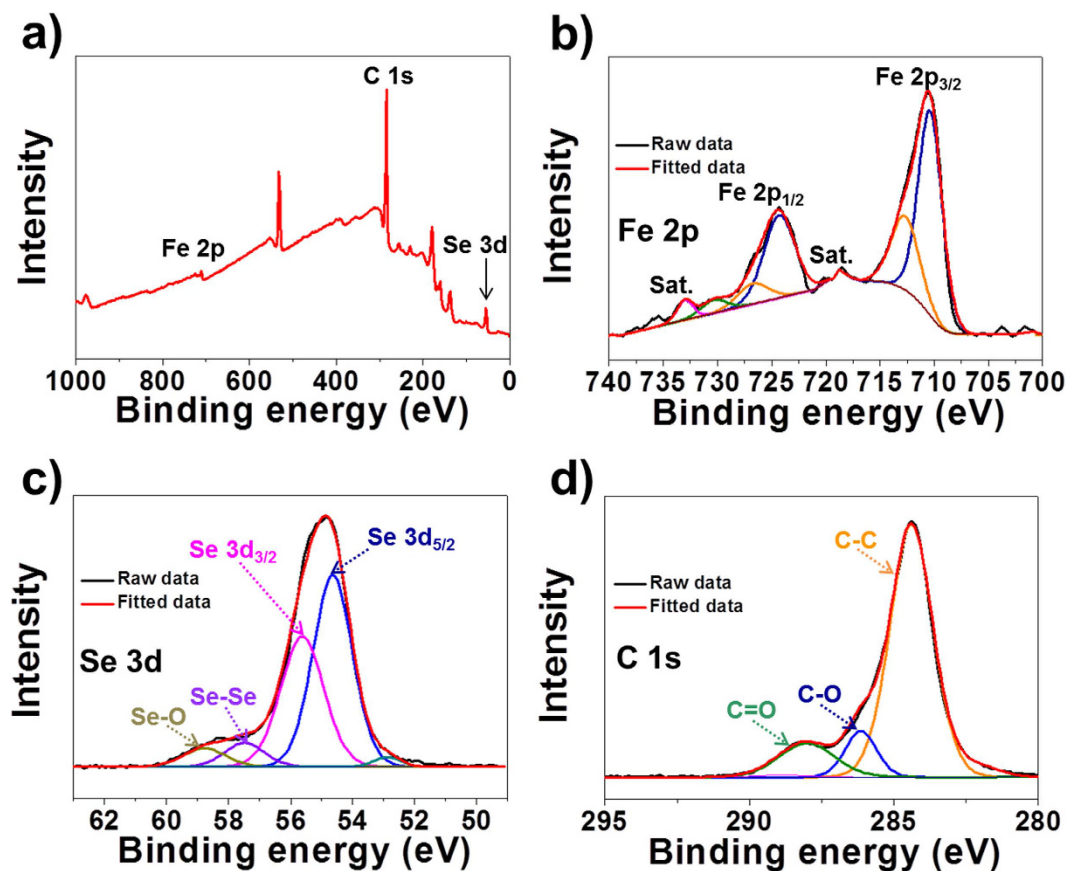


**Figure 4.** XPS spectra of the hollow  $\text{FeSe}_x$ -decorated rGO composite powders: (a) wide-scan XPS spectrum, (b) Fe 2p, (c) Se 3d, and (d) C 1s.

two reduction peaks located at 0.8 and 0.4 were attributed to the formation of  $\text{FeSe}$  and  $\text{Na}_2\text{Se}$ , and Fe and  $\text{Na}_2\text{Se}$ , respectively<sup>28</sup>. During the anodic scans, two oxidation peaks were observed at 1.6 and 2.0 V, which were attributed to the formation of  $\text{Na}_x\text{FeSe}_2$  and  $\text{FeSe}_2$ , respectively<sup>28</sup>. The first cathodic scan of the  $\text{Fe}_2\text{O}_3$ -rGO composite powders shown in Fig. 6b revealed a broad weak peak at around 0.5 V, which might be attributed to the reduction of Fe (III) to Fe (0)<sup>33</sup>. The initial discharge and charge curves of the  $\text{Fe}_2\text{O}_3$ -rGO composite powders shown in Fig. 6c also did not show distinct plateaus. The initial discharge and charge curves of the composite powders obtained after selenization at different times at a constant current density of  $0.3 \text{ A g}^{-1}$  are shown in Fig. 6c. The selenization of the composite powders did not occur at a short selenization time of 10 min as confirmed by XRD pattern shown in Fig. S6. Therefore, the clear plateaus in the initial discharge and charge curves were not observed for the sample obtained after selenization for 10 min. Unclear plateaus were also observed in the initial discharge and charge curves of the  $\text{FeSe}_x$ -rGO composite powders obtained after selenization for 1 h, in which complete selenization of the composite powders was achieved. However, the initial discharge and charge curves of the  $\text{FeSe}_x$ -rGO composite powders obtained after selenization for 6 h showed clear plateaus, as indicated by arrows in Fig. 6c. The crystal growth of the  $\text{FeSe}_x$  phase during the long-term selenization process resulted in clear plateaus in their initial discharge and charge curves. The initial discharge capacities of the composite powders obtained after selenization for 10 min, 1 h, and 6 h were 444, 598, and 625  $\text{mA h g}^{-1}$ , respectively, and their corresponding charge capacities were 235, 408, and 447  $\text{mA h g}^{-1}$ , respectively. The complete conversion of the metallic Fe to the  $\text{FeSe}_x$  phase increased the initial discharge and charge capacities of the composite powders. The cycling performances of the composite powders obtained after selenization for different times at a constant current density of  $0.3 \text{ A g}^{-1}$  are shown in Fig. 6d. The  $\text{FeSe}_x$ -rGO composite powders obtained after selenization for 6 h had superior cycling performance compared to that of the composite powders obtained after selenization for 1 h. The long-term selenization process for 6 h improved the sodium-ion storage properties of the  $\text{FeSe}_x$ -rGO composite powders by improving the crystallinity. The discharge capacities of the  $\text{FeSe}_x$ - and  $\text{Fe}_2\text{O}_3$ -rGO composite powders obtained after the post-treatment process for 6 h were 434 and 174  $\text{mA h g}^{-1}$ , respectively, for the 200<sup>th</sup> cycle at a current density of  $0.3 \text{ A g}^{-1}$ . The rate performance of the  $\text{FeSe}_x$ -rGO composite powders obtained after selenization for 6 h is shown in Fig. 6e, in which the current density increases in a step-wise manner from 0.2 to  $5 \text{ A g}^{-1}$ . The composite powders had final discharge capacities of 478, 423, 377, 324, 294, 270, and 250  $\text{mA h g}^{-1}$  at current densities of 0.2, 0.5, 1, 2, 3, 4, and  $5 \text{ A g}^{-1}$ , respectively. The discharge capacity of the composite powders recovered well to  $504 \text{ mA h g}^{-1}$  when the current density was returned to  $0.2 \text{ A g}^{-1}$  after cycling at high current densities. The long-term cycling performance of the  $\text{FeSe}_x$ -rGO composite powders obtained after selenization for 6 h is shown

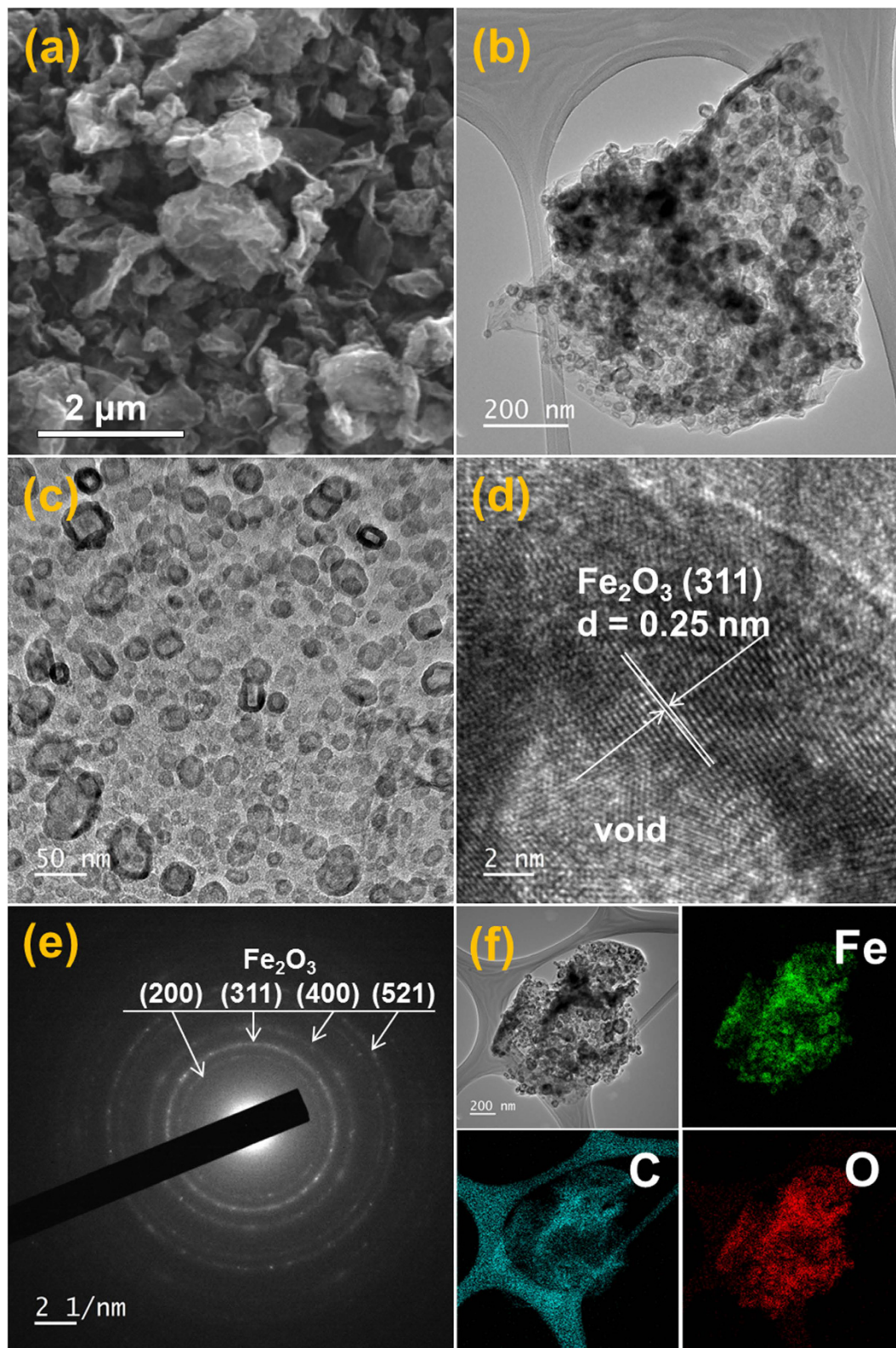


**Figure 5.** Morphologies, SAED pattern, and elemental mapping images of the hollow  $\text{Fe}_2\text{O}_3$ -decorated rGO composite powders obtained by nanoscale Kirkendall diffusion: (a) SEM image, (b,c) TEM images, (d) HR-TEM image, (e) SAED pattern, and (f) elemental mapping images.

in Fig. 6f for a high current density of  $1 \text{ A g}^{-1}$ . The discharge capacities of the 2<sup>nd</sup> and 1000<sup>th</sup> cycles were  $402.0$  and  $311.4 \text{ mA h g}^{-1}$ , respectively, and the capacity retention measured from the second cycle was 77%.

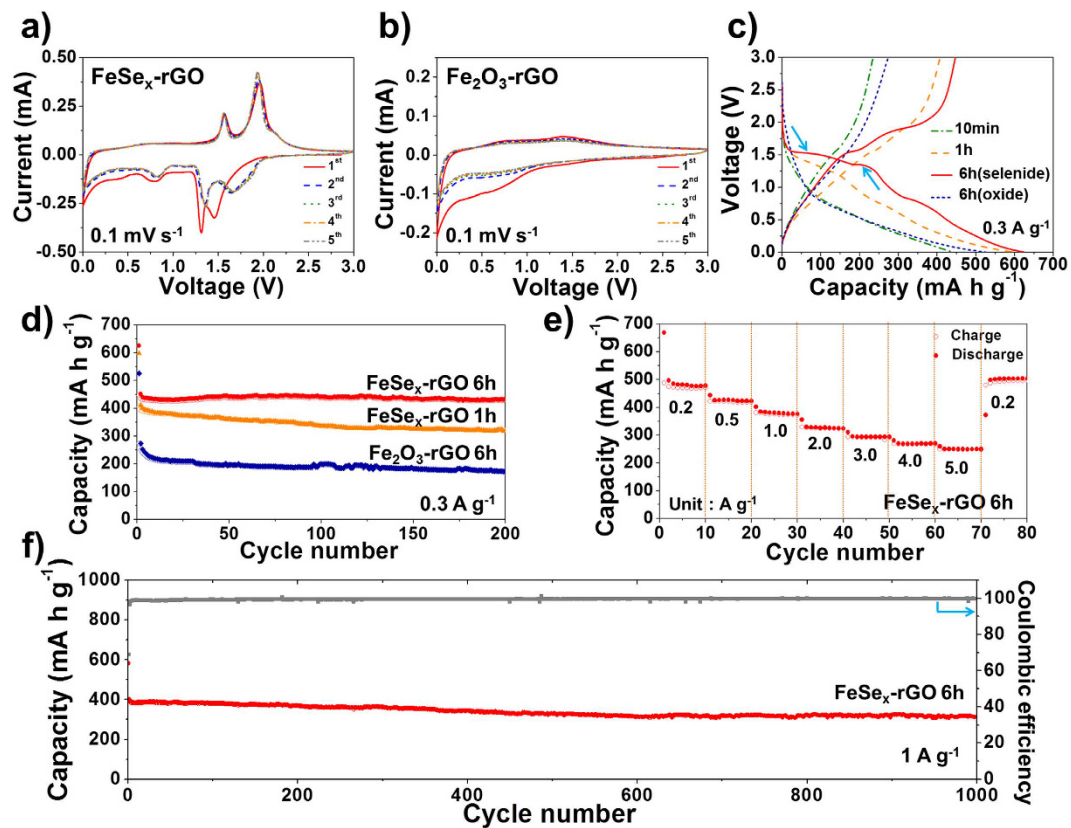


**Figure 6.** Electrochemical properties of the hollow  $\text{FeSe}_x$ - and  $\text{Fe}_2\text{O}_3$ -decorated rGO composite powders: (a) CV curves of  $\text{FeSe}_x$ -rGO, (b) CV curves of  $\text{Fe}_2\text{O}_3$ -rGO, (c) initial charge-discharge curves, (d) cycling performances, (e) rate performance, and (f) long term cycling performance.

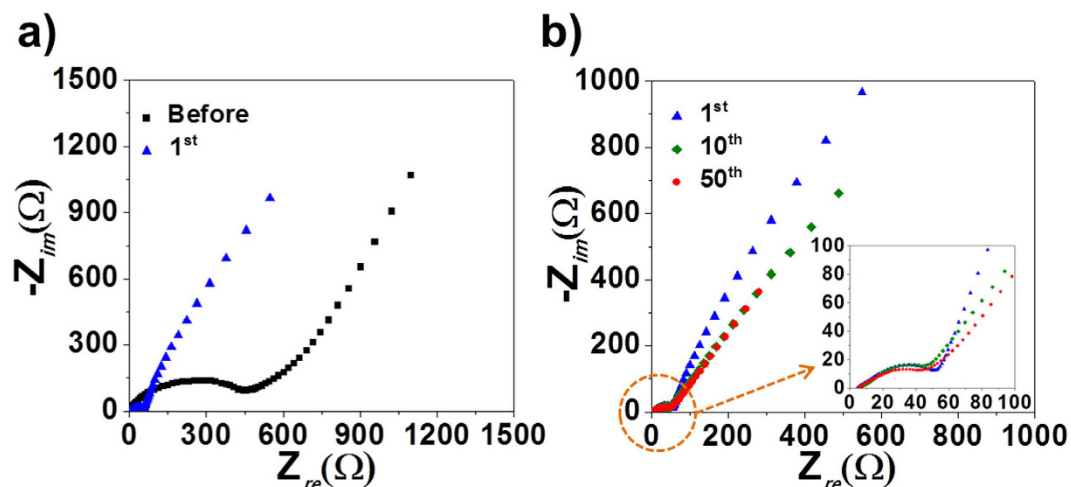


**Figure 7.** Nyquist impedance plots of the hollow  $\text{FeSe}_x$ -decorated rGO composite powders: (a) before and after 1 cycle and (b) after 1, 10, and 50 cycles.

The excellent sodium-ion storage properties of the  $\text{FeSe}_x$ -rGO composite powders obtained after selenization for 6h were confirmed by electrochemical impedance spectroscopy (EIS) measurements, as shown in Fig. 7. EIS measurements were performed on the composite powders before and after 1, 10, and 50 cycles. The Nyquist plots display compressed semicircles in the medium-frequency range, which indicate the charge-transfer resistance ( $R_{ct}$ ) of the electrode<sup>34–36</sup>. The charge-transfer resistance of the  $\text{FeSe}_x$ -rGO composite powders decreased after the first cycle due to the formation of ultrafine nanocrystals during initial cycling. The low charge-transfer resistance of the electrode was maintained even after 50 cycles due to the high structural stability of the  $\text{FeSe}_x$ -rGO composite powders for repeated sodium-ion charge and discharge processes.



## Conclusions

This paper is the first report of the synthesis of nanostructured iron selenide materials decorated within the crumpled rGO matrix and their electrochemical properties as NIB anode materials. Metallic Fe-rGO composite powders transformed into FeSe<sub>x</sub>-rGO composite powders by a simple selenization process with H<sub>2</sub>Se gas, in which the nanoscale Kirkendall diffusion process changed the densely structured Fe nanocrystals into hollow FeSe<sub>x</sub> nanospheres. The FeSe<sub>x</sub>-rGO composite powders showed excellent long-term cycling performance at a high current density of 1 A g<sup>-1</sup> and good rate performance for sodium-ion storage. The simple process developed in this study could be applied in the preparation of uniquely structured metal selenide-rGO composite powders with various compositions for wide applications including sodium-ion batteries.

## Materials and Methods

**Sample preparation.** A three-step process was applied to the preparation of hollow FeSe<sub>x</sub> nanoparticles-decorated rGO composite powders. Iron oxide-decorated rGO composite powders were prepared by a simple spray pyrolysis process using a spray solution of iron nitrate nonahydrate (Fe(NO<sub>3</sub>)<sub>3</sub>·9H<sub>2</sub>O) and graphene oxide (GO) nanosheets. GO nanosheets were synthesized from graphite flakes using a modified Hummers method, as described in our previous report<sup>29</sup>. As-synthesized GO nanosheets were re-dispersed in distilled water and then exfoliated by ultrasonication. 0.015 M of Fe(NO<sub>3</sub>)<sub>3</sub>·9H<sub>2</sub>O was dissolved in 500 mL of 1 mg mL<sup>-1</sup> exfoliated GO dispersion to fabricate iron oxide-decorated rGO composite powders. In the spray pyrolysis process, droplets were generated using a 1.7-MHz ultrasonic spray generator consisting of six vibrators. The droplets were carried to a quartz reactor with length of 1200 mm and diameter of 50 mm, using N<sub>2</sub> as the carrier gas at a flow rate of 10 L min<sup>-1</sup>. The reactor temperature was maintained at 400 °C. The first step in the post-treatment process was carried out at 400 °C for 3 h under a 10% H<sub>2</sub>/Ar reducing atmosphere; this produced metallic Fe nanopowder-decorated rGO composite powders. The second step in the post-treatment process of the metallic Fe nanopowder-decorated rGO composite powders was carried out at 300 °C for 6 h in H<sub>2</sub>Se gas, which was formed from commercial selenium metal powders by hydrogen gas, to produce hollow FeSe<sub>x</sub> nanoparticles-decorated rGO composite powders. For the selenization process, the metallic Fe nanopowder-decorated rGO composite powders and selenium metal powders were loaded in a covered alumina boat and placed in a quartz tube reactor. The post-treatment process of the metallic Fe nanopowder-decorated rGO composite powders at 300 °C for 6 h under air atmosphere produced hollow Fe<sub>2</sub>O<sub>3</sub> nanoparticles-decorated rGO composite powders.

**Characterization.** The crystal structures of the composite powders were investigated using X-ray diffraction (XRD, X'pert PRO MPD) with Cu-K<sub>α</sub> radiation (λ = 1.5418 Å) at the Korea Basic Science Institute (Daegu). The morphologies of the powders were investigated using field-emission scanning electron microscopy (FE-SEM, Hitachi S-4800) and high-resolution transmission electron microscopy (HR-TEM, JEOL JEM-2100F) at a working voltage of 200 kV. X-ray photoelectron spectroscopy (XPS) of the powders was performed using an ESCALAB-250 with Al K<sub>α</sub> radiation (1486.6 eV). To determine the amount of rGO in the hollow FeSe<sub>x</sub> nanoparticles-decorated rGO composite powders, thermogravimetric analysis (TGA, SDT Q600) was performed in air at a heating rate of 10 °C min<sup>-1</sup>.

**Electrochemical measurements.** The electrochemical properties of the powders were analyzed using a 2032-type coin cell. The anode was prepared by mixing the active material, carbon black, and sodium carboxymethyl cellulose in a weight ratio of 7:2:1. Stick-type sodium metal and microporous polypropylene film were used as the counter electrode and separator, respectively. The separators (Welcos Co., Ltd., Korea) were microporous monolayer polypropylene membranes, with a thickness of 22 μm. The electrolyte was 1 M NaClO<sub>4</sub> (Aldrich) dissolved in a mixture of ethylene carbonate/dimethyl carbonate (EC/DMC; 1:1 v/v, PURIEL), to which 5 wt% fluoroethylene carbonate (FEC) was added. The discharge/charge characteristics of the samples were investigated by cycling in the potential range of 0.001–3 V at various current densities. Cyclic voltammograms (CVs) were measured at a scan rate of 0.1 mV s<sup>-1</sup>. The dimensions of the anode were 1 cm × 1 cm and the mass loading was approximately 1.2 mg cm<sup>-2</sup>. The electrochemical impedance was measured using electrochemical impedance spectroscopy (EIS) over the frequency range of 0.01 Hz–100 kHz.

## References

- Gao, M. R., Xu, Y. F., Jiang, J. & Yu, S. H. Nanostructured metal chalcogenides: synthesis, modification, and applications in energy conversion and storage devices. *Chem. Soc. Rev.* **42**, 2986–3017 (2013).
- Pumera, M., Sofer, Z. & Ambrosi, A. Layered transition metal dichalcogenides for electrochemical energy generation and storage. *J. Mater. Chem. A* **2**, 8981–8987 (2014).
- Acerce, M., Voiry, D. & Chhowalla, M. Metallic 1T phase MoS<sub>2</sub> nanosheets as supercapacitor electrode materials. *Nat. Nanotech.* **10**, 313–318 (2015).
- Muller, G. A., Cook, J. B., Kim, H. S., Tolbert, S. H. & Dunn, B. High performance pseudocapacitor based on 2D layered metal chalcogenide nanocrystals. *Nano Lett.* **15**, 1911–1917 (2015).
- Xia, C. & Alshareef, H. N. Self-templating scheme for the synthesis of nanostructured transition-metal chalcogenide electrodes for capacitive energy storage. *Chem. Mater.* **27**, 4661–4668 (2015).
- Yang, J. *et al.* Two-dimensional hybrid nanosheets of tungsten disulfide and reduced graphene oxide as catalysts for enhanced hydrogen evolution. *Angew. Chem. Int. Ed.* **52**, 13751–13754 (2013).
- Zhang, J., Wang, Q., Wang, L. H., Li, X. & Huang, W. Layer-controllable WS<sub>2</sub>-reduced graphene oxide hybrid nanosheets with high electrocatalytic activity for hydrogen evolution. *Nanoscale* **7**, 10391–10397 (2015).
- Kim, Y. J. *et al.* Tin phosphide as a promising anode material for Na-ion batteries. *Adv. Mater.* **26**, 4139–4144 (2014).
- Jang, J. Y. *et al.* Interfacial architectures based on a binary additive combination for high-performance Sn<sub>4</sub>P<sub>3</sub> anodes in sodium-ion batteries. *J. Mater. Chem. A* **3**, 8332–8338 (2015).
- Choi, S. H., Ko, Y. N., Lee, J. K. & Kang, Y. C. 3D MoS<sub>2</sub>-graphene microspheres consisting of multiple nanospheres with superior sodium ion storage properties. *Adv. Funct. Mater.* **25**, 1780–1788 (2015).

11. Wu, R. B. *et al.* MOFs-derived copper sulfides embedded within porous carbon octahedra for electrochemical capacitor applications. *Chem. Commun.* **51**, 3109–3112 (2015).
12. Xu, X. J., Ji, S. M., Gu, M. Z. & Liu, J. *In situ* synthesis of MnS hollow microspheres on reduced graphene oxide sheets as high-capacity and long-life anodes for Li- and Na-ion batteries. *ACS Appl. Mater. Interfaces* **7**, 20957–20964 (2015).
13. Liu, P. *et al.* Bundle-like  $\alpha'$ -NaV<sub>2</sub>O<sub>5</sub> mesocrystals: from synthesis, growth mechanism to analysis of Na-ion intercalation/deintercalation abilities. *Nanoscale* **8**, 1975–1985 (2016).
14. Zhu, Y. *et al.* Electrospun Sb/C Fibers for a Stable and Fast Sodium-Ion Battery Anode. *ACS Nano* **7**, 6378–6386 (2013).
15. Wang, H. *et al.* Phase transition mechanism and electrochemical properties of nanocrystalline MoSe<sub>2</sub> as anode materials for the high performance lithium-ion battery. *J. Phys. Chem. C* **119**, 10197–10205 (2015).
16. Im, H. S. *et al.* Germanium and tin selenide nanocrystals for high-capacity lithium ion batteries: Comparative phase conversion of germanium and tin. *J. Phys. Chem. C* **118**, 21884–21888 (2014).
17. Zhang, Z., Fu, Y., Yang, X., Qu, Y. H. & Li, Q. Nanostructured ZnSe anchored on graphene nanosheets with superior electrochemical properties for lithium ion batteries. *Electrochim. Acta* **168**, 285–291 (2015).
18. Han, G. *et al.* In<sub>3</sub>Se<sub>4</sub> and S-doped In<sub>3</sub>Se<sub>4</sub> nano/micro-structures as new anode materials for Li-ion batteries. *J. Mater. Chem. A* **3**, 7560–7567 (2015).
19. Ko, Y. N., Choi, S. H., Park, S. B. & Kang, Y. C. Hierarchical MoSe<sub>2</sub> yolk-shell microspheres with superior Na-ion storage properties. *Nanoscale* **6**, 10511–10515 (2014).
20. Saha, P. *et al.* Electrochemical performance of chemically and solid state-derived chevrel phase Mo<sub>6</sub>T<sub>8</sub> (T = S, Se) positive electrodes for sodium-ion batteries. *J. Phys. Chem. C* **119**, 5771–5782 (2015).
21. Yue, J. L., Sun, Q. & Fu, Z. W. Cu<sub>2</sub>Se with facile synthesis as a cathode material for rechargeable sodium batteries. *Chem. Commun.* **49**, 5868–5870 (2013).
22. Kim, Y. J. *et al.* SnSe alloy as a promising anode material for Na-ion batteries. *Chem. Commun.* **51**, 50–53 (2015).
23. Zhang, Z., Fu, Y., Yang, X., Qu, Y. H. & Zhang, Z. Y. Hierarchical architectural MoSe<sub>2</sub> nanosheets/graphene composites as anodes for lithium-ion and sodium-ion batteries with enhanced electrochemical performance. *Chem. Nano. Mat.* **1**, 409–414 (2015).
24. Azizi, A. *et al.* Freestanding van der waals heterostructures of graphene and transition metal dichalcogenides. *ACS Nano* **9**, 4882–4890 (2015).
25. Lin, Y. C. *et al.* Atomically thin heterostructures based on single-layer tungsten diselenide and graphene. *Nano Lett.* **14**, 6936–6941 (2014).
26. Xie, J. *et al.* *In situ* TEM characterization of single PbSe/reduced-graphene-oxide nanosheet and the correlation with its electrochemical lithium storage performance. *Nano Energy* **5**, 122–131 (2014).
27. Zhang, X., Yang, Y. X., Guo, S. Q., Hu, F. Z. & Liu, L. Mesoporous Ni<sub>0.85</sub>Se nanospheres grown *in situ* on graphene with high performance in dye-sensitized solar cells. *ACS Appl. Mater. Interfaces* **7**, 8457–8464 (2015).
28. Zhang, K., Hu, Z., Liu, Tao, Z. L. & Chen, J. FeSe<sub>2</sub> microspheres as a high-performance anode material for Na-ion batteries. *Adv. Mater.* **27**, 3305–3309 (2015).
29. Choi, S. H. & Kang, Y. C. Crumpled graphene–molybdenum oxide composite powders: Preparation and application in lithium-ion batteries. *ChemSusChem* **7**, 523–528 (2014).
30. Liu, K. W. *et al.* Electronic and magnetic properties of FeSe thin film prepared on GaAs (001) substrate by metal-organic chemical vapor deposition. *Appl. Phys. Lett.* **90**, 262503 (2007).
31. Zheng, Q. L., Cheng, X. & Li, H. Y. Microwave synthesis of high activity FeSe<sub>2</sub>/C catalyst toward oxygen reduction reaction. *Catalysts* **5**, 1079–1091 (2015).
32. Wang, Q. Q. *et al.* Growth of nickel silicate nanoplates on reduced graphene oxide as layered nanocomposites for highly reversible lithium storage. *Nanoscale* **7**, 16805–16811 (2015).
33. Zhang, N. *et al.* 3D porous  $\gamma$ -Fe<sub>2</sub>O<sub>3</sub>@C nanocomposite as high-performance anode material of Na-ion batteries. *Adv. Energy Mater.* **5**, doi: 10.1002/aenm. 201401123 (2015).
34. Rahman, M. M. *et al.* *Ex situ* electrochemical sodiation/desodiation observation of Co<sub>3</sub>O<sub>4</sub> anchored carbon nanotubes: a high performance sodium-ion battery anode produced by pulsed plasma in a liquid. *Nanoscale* **7**, 13088–13095 (2015).
35. Zhong, Y. *et al.* Orderly packed anodes for high-power lithium-ion batteries with super-long cycle life: rational design of MnCO<sub>3</sub>/large-area graphene composites. *Adv. Mater.* **27**, 806–812 (2015).
36. Xin, F. X. *et al.* Enhanced Electrochemical Performance of Fe<sub>0.71</sub>Sn<sub>2</sub>@Reduced Graphene Oxide Nanocomposite Anodes for Both Li-Ion and Na-Ion Batteries. *ACS Appl. Mater. Interfaces* **7**, 7912–7919 (2015).

## Acknowledgements

This work was supported by the Energy Efficiency & Resources Core Technology Program of the Korea Institute of Energy Technology Evaluation and Planning (KETEP), granted financial resource from the Ministry of Trade, Industry & Energy, Republic of Korea (201320200000420). This work was supported by a National Research Foundation of Korea (NRF) grant funded by the Korea government (MEST) (NRF-2015R1A2A1A15056049). This research was supported by a grant from the Intelligent Synthetic Biology Center of Global Frontier Project (2011-0031955) funded by the Ministry of Science, ICT and Future Planning, Republic of Korea.

## Author Contributions

G.D.P., J.S.C. and Y.C.K. devised the concept, designed the experiment, and wrote the manuscript. G.D.P. and J.S.C. performed the experiments and analyzed the data. Y.C.K. and J.K.L. supervised the project. All authors discussed the results and contributed in this manuscript.

## Additional Information

**Supplementary information** accompanies this paper at <http://www.nature.com/srep>

**Competing financial interests:** The authors declare no competing financial interests.

**How to cite this article:** Park, G. D. *et al.* Na-ion Storage Performances of FeSe<sub>x</sub> and Fe<sub>2</sub>O<sub>3</sub> Hollow Nanoparticles-Decorated Reduced Graphene Oxide Balls prepared by Nanoscale Kirkendall Diffusion Process. *Sci. Rep.* **6**, 22432; doi: 10.1038/srep22432 (2016).



This work is licensed under a Creative Commons Attribution 4.0 International License. The images or other third party material in this article are included in the article's Creative Commons license, unless indicated otherwise in the credit line; if the material is not included under the Creative Commons license, users will need to obtain permission from the license holder to reproduce the material. To view a copy of this license, visit <http://creativecommons.org/licenses/by/4.0/>